Journal of Materials Chemistry C

PAPER

View Article Online
View Journal | View Issue

Cite this: J. Mater. Chem. C, 2016, 4, 6401

Scalable production of $CuInS_2$/ZnS quantum dots in a two-step droplet-based microfluidic platform†

Alexandra Yashina,‡[a] Ioannis Lignos,‡[a] Stavros Stavrakis,[a] Jaebum Choo[b] and Andrew J. deMello*[a]

Received 18th May 2016,
Accepted 15th June 2016

DOI: 10.1039/c6tc02057g

www.rsc.org/MaterialsC

We report the scalable formation of $CuInS_2$/ZnS nanocrystals using a two-stage microfluidic reactor integrated with a real-time optical detection system, which is able to monitor reaction parameters prior and subsequent to the addition of the shell material. By injecting a ZnS single source precursor in droplets containing $CuInS_2$ cores and without the need of purification steps, we are able to obtain core–shell nanocrystal populations emitting between 580 and 760 nm with significant narrower size distributions (90–95 nm) than for the same material systems synthesized on the macroscale. In-line monitoring allowed for rapid assessment of optimum reaction parameters (Cu/In, S/(Cu + In), Zn/(Cu + In) molar ratios, temperatures and reaction time) and enabled the formation of $CuInS_2$/ZnS nanocrystals with high photoluminescence quantum yields (~55%) within a few seconds. We believe that this synthetic methodology will be of significant utility in controllable production of ternary and quaternary metal chalcogenides, complex core–shell and doped nanostructures.

Introduction

Investigation of effective strategies for the controlled formation of non-heavy metal semiconductor nanocrystals (NCs) is of high current interest with regard to replacing toxic binary Cd- or Pb-chalcogenides commonly used in optoelectronic devices and biological imaging applications.[1,2] In this respect, much effort has focused on the synthesis and characterization of multinary I–III–VI_2 chalcogenides[3] including $CuInS_2$,[4–13] $CuInSe_2$,[14–18] $AgInS_2$,[6,19–22] and Cu_2ZnSnS_4.[23–26] An intrinsic advantage of such compounds when compared to binary non-heavy metal chalcogenides is the tunability of their emission across the visible to near IR regions of the electromagnetic spectrum through control of particle size. Of all reported Cd- and Pb-free NCs, $CuInS_2$ NCs have received perhaps the most attention since they are recognized to be attractive candidate components in film solar cells and light-emitting devices, and well-suited to use as *in vivo* biological probes.[3,27] $CuInS_2$ NCs have a relatively narrow bandgap (1.53 eV) along with tunable emission between 550 and 850 nm but typically exhibit low photoluminescence quantum yields (10%) due to the preponderance of surface defects. However, efficient surface passivation with a wide gap shell-material, such as ZnS, leads to the formation of highly-photostable $CuInS_2$/ZnS NCs with photoluminescence quantum yields (QYs) reaching up to 80%.[28–31]

Unfortunately, the robust synthesis of $CuInS_2$/ZnS NCs of defined composition with the controllable addition of multiple ZnS monolayers remains a complex and time-consuming challenge.[3,27] Unsurprisingly, the synthesis of $CuInS_2$/ZnS in conventional macroscale reactors results in NCs with properties (such as average particle size, population size distribution and photoluminescence quantum yield) that vary from batch-to-batch due to unavoidable variations in environmental conditions within the reactor. More importantly the addition of supplementary reagents required for the formation of core–shell structures remains a complex undertaking,[32,33] since shell growth is ideally achieved by successive ion layer adhesion and reaction (SILAR), which requires core particle purification and its transfer to a second reactor for shell growth.[34] Accordingly, such requirements increase processing timescales and hinder the scalable production of multinary composites with binary shells.

Over the past decade, microfluidic reactors have shown great promise in engendering the controlled and on-demand production of complex NC structures with uniform physicochemical properties.[32,33,35,36] Rapid mass and heat transfer in microfluidic environments, efficient decoupling of nucleation and

[a] Institute for Chemical and Bioengineering, Department of Chemistry and Applied Biosciences, ETH Zürich, Vladimir-Prelog-Weg 1 8093, Zürich, Switzerland. E-mail: andrew.demello@chem.ethz.ch; Tel: +41 44 633 66 10

[b] Department of Bionano Technology, Hanyang University, Ansan 15588, Republic of Korea

† Electronic supplementary information (ESI) available. See DOI: 10.1039/c6tc02057g

‡ These authors contributed equally to this work.

growth stages, facile multi-step addition of reagents and fast parametric screening of reaction parameters for rapid reaction optimization are major advantages when compared to conventional macroscale (batch) reactors. Indeed, continuous microfluidic syntheses of semiconductor NCs with core–shell morphologies have already been reported, including the formation of CdS/ZnS,[37–39] CdSe/ZnS,[39,40] CdTe/ZnS,[40] ZnSe/ZnS,[41] InP/ZnS,[42] CdSe/CdS/ZnS,[37] CdSeS/ZnS,[37] Cu–In–(Zn)–S/ZnS[43,44] and Ag–In–Zn–S/ZnS[44] NCs. Unfortunately, the effectiveness of continuous flow microfluidic reactors in generating core–shell NCs of defined size and composition is somewhat compromised by the interaction of fluid with the microfluidic channel.[32,33] Furthermore the parabolic velocity profiles established over the cross-section of the channel generate a significant (and unavoidable) residence-time distribution that in turn leads to NCs of varying size. This is particularly problematic in the synthesis of core–shell NCs, since the formation of well-defined core–shell structures requires the delivery of both low and precise concentrations of shell composites to avoid secondary nucleation. These limitations can be suppressed (or even eliminated) through the use of segmented-flow (or droplet-based) microfluidic reactors and multi-step dosing of reagents.[32,33] Recently, droplet-based microfluidic platforms integrated with on-line analytics and optimization algorithms have shown significant utility in optimizing the processes of various NCs (CdSe,[45,46] CdSeTe,[45] PbS,[47,48] PbSe,[47] Cs-based perovskites[49]) and allowing excellent size control and reaction reproducibility. In addition, such systems allow isolation of the reaction mixture for formation of core particles and at the same time enable precise addition of the shell material into individual droplets, either by droplet-merging[50] or direct injection,[51,52] to ensure the controlled formation of multiple-layer shell deposition on the surface of the core.[33,53] Interestingly, multi-step synthesis in droplet-based formats for the synthesis of core–shell semiconductor NCs has rarely been reported.[54] This is most likely due to the fact that dosing droplets with specific amounts of reagents remains a non-trivial operation. Indeed, to our knowledge there has been only one literature report describing the multistep dosing of individual droplets for the sequential growth of NCs.[52]

Herein, we report the design and construction of a two-stage droplet-based microfluidic platform for the controlled synthesis of $CuInS_2$/ZnS NCs. Such a platform allows for precise control over reaction parameters such as the temperature (up to 240 °C) for $CuInS_2$ synthesis and ZnS shell growth, reaction times (of between 2 and 3 minutes) in both reaction stages and independent adjustment of Cu/In, S/(Cu + In) and Zn/(Cu + In) molar ratios for the synthesis of size-tunable and photostable $CuInS_2$/ZnS NCs. The microfluidic platform allows for the continuous formation of core–shell $CuInS_2$/ZnS NCs by direct injection of shell material to each individual droplet containing $CuInS_2$ NCs without the need for purification of the core particles. Moreover, an integrated photoluminescence optical detection system allows real-time screening of material properties before and after shell growth. The resulting $CuInS_2$/ZnS NCs exhibit tunable emission between 580 and 760 nm and are characterized by narrow emission linewidths between 90 and 105 nm. Additionally, the resulting photoluminescence quantum yields for $CuInS_2$ and $CuInS_2$/ZnS NCs are 12% and 55% respectively.

Experimental

Chemicals

Copper(I) iodide (CuI, 99.999%), indium(III) acetate ($In(OAc)_3$, 99.99%), sulfur (S), 1-dodecanethiol (DDT, 98%), 1-octadecene (ODE, 90%), zinc acetate ($Zn(OAc)_2$, 99.99%) oleic acid (OA, 90%), oleylamine (OLA, 90%), ethanol over molecular sieve ($H_2O \leq 0.01\%$), and *n*-hexane absolute over molecular sieve ($H_2O \leq 0.01\%$) were purchased form Sigma-Aldrich, Switzerland. Anhydrous toluene (99.8%) was purchased from ABCR Chemicals, Germany. Galden PFPE carrier fluid was purchased from Blaser Swisslube AG, Germany.

Preparation of precursors

$CuInS_2$ synthesis. For the copper precursor solution, CuI (0.095 g, 0.5 mmol) and OLA (0.5 mL) were mixed with ODE (3.3 mL) in a three-neck flask and stirred at 120 °C for 90 minutes under argon. For the indium precursor solution $In(OAc)_3$ (0.15 g, 0.5 mmol), OA (0.35 mL) and OLA (0.15 mL) were mixed with ODE (3.3 mL) in a three neck flask and stirred at 120 °C for 90 minutes under argon. For the sulfur solution, S (0.032 g, 1 mmol), DDT (1 mL) and ODE (4 mL) were stirred at 120 °C for 90 minutes under argon in a three neck flask. After cooling, all three solutions and the Galden carrier fluid were loaded into 10 mL gastight glass syringes.

$CuInS_2$/ZnS synthesis. The Cu, In and S precursor solutions were prepared in the exact same manner as described previously. For the zinc solution, $Zn(OAc)_2$ (0.36 g, 4 mmol) and OLA (1 mL) were mixed with ODE (4 mL) in a three-neck flask and stirred at 160 °C for 20 minutes under argon. The solution was then allowed to cool and then loaded into a 10 mL gastight glass syringe.

Reactor design

Precision syringe pumps (neMESYS Low Pressure Syringe Pumps, Cetoni GmbH, Germany) were used to inject the dispersed phase into a PEEK cross (P-729, Upchurch Scientific, Germany) for initial mixing of the reagent solutions. Subsequently, the solution and the carrier fluid (Galden, Blaser Swisslube AG, Germany) were directed to a PEEK T-junction (P-727 PEEK Tee, Upchurch Scientific, Germany) to form 20–30 nanoliter volume droplets. Typical flow rates for the carrier phase were 25–100 μL min^{-1} and 10–50 μL min^{-1} for the dispersed phase. The cross, the T-junction and the syringes carrying the precursor solutions were connected through PTFE tubing (ID 250 μm, OD 1/16″, Upchurch Scientific, Germany) using PEEK fingertight fittings (F-127, Upchurch Scientific, Germany). The carrier fluid was transferred to the PEEK cross through FEP tubing (ID 750 μm, OD 1/16″, Upchurch Scientific, Germany). The formed droplets containing the reaction mixture were subsequently directed through PTFE tubing (ID 500 μm, OD 1/16″, Upchurch Scientific, Germany) coiled around a

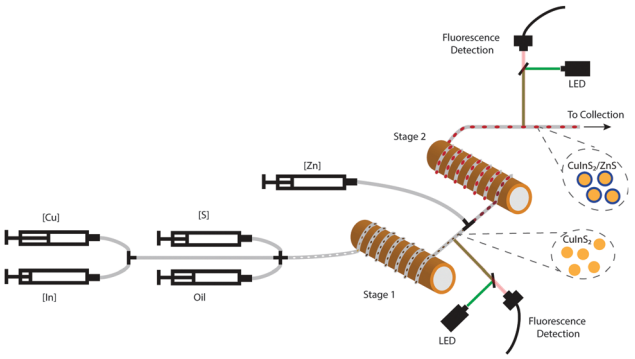

Fig. 1 Two-stage droplet-based microfluidic platform for the controlled synthesis of $CuInS_2$/ZnS NCs.

copper-heating rod (diameter = 1.5 cm) (Stage 1) to allow the initiation of reaction of the $CuInS_2$ NCs (core NCs) (Fig. 1). The droplets containing the $CuInS_2$ NC solution were directed *via* a high-purity PFA tubing (OD 1/16″, ID 500 μm) (for characterization of the synthesized cores) to another T-junction (P-727 PEEK Tee, Upchurch Scientific, Germany) where a solution of Zn precursor was injected into each droplet. After the addition of the Zn precursor droplets were transported through PFA tubing (ID 500 μm, OD 1/16″, Upchurch Scientific, Germany) coiled around a second copper-heating rod (diameter = 1.5 cm) (Stage 2) for ZnS shell growth. Finally, high-purity PFA tubing (OD 1/16″, ID 500 μm) was connected with the PTFE tubing for a second characterization measurement. The temperature of both copper rods was controlled independently using two heating cartridges (6.5 × 40 mm, 100 W, Farnell, Switzerland), embedded inside the heating rods. Both temperatures were monitored using thermocouples (Sensor, Thermoelement Type K – 0.5 mm, Farnell, Switzerland), which were inserted into the copper blocks close to the surface. Temperature control was realized using two PID controllers (CN7800, Omega, USA) with an observed temperature variation from the set point of less than 0.1 °C. The formed droplets can be rapidly heated to the desired reaction temperature within 100 ms.[49] Control over the reaction time is achieved by controlling the residence time of the droplets in the heated zones.

Two-stage photoluminescence detection

The detection system consists of two identical photoluminescence detectors, located after the synthesis of the core NC solution and after the growth of the shell (Fig. 1). For simplicity, only one of the photoluminescence detection systems is now described. A UV LED (M405L2-UV Mounted LED, 1000 mA, 410 mW, Thorlabs, Germany) was used as an excitation source. The collimated beam was directed towards a dichroic beam splitter (ZT405rdc-UF1, Chroma, Germany) and then focused into the microfluidic channel using an aspheric lens (A240TM-f = 8.0 mm – NA 0.50, Thorlabs, Germany). Emission originating from the microfluidic channel was then collected by the same lens, passed through the dichroic beam splitter, a long-pass filter (442 LP Edge Basic Longpass-Filter, AHF, Germany) and coupled *via* a 10× objective (RMS10× – NA 0.25, Thorlabs, Germany) to a fiber spectrometer (PRo+, Ocean Optics, UK) through a 2 m long multimode fiber with a core diameter of 400 μm (QP100-2-UV-VIS, Ocean Optics, UK). The spectrometer comprised a 20 μm entrance slit, a 600 lines mm^{-1} grating and a detector containing 2048 pixels. The spectrometer was operated between 400 and 1100 nm, and data recorded using a 100 ms integration time. The UV LEDs for both detection systems were controlled using LED drivers (T-Cube LED Driver 1200 mA with Trigger Mode) which were externally controlled by home-made LabView software, which triggers the excitation sources in an alternate fashion and with a time interval of several seconds, allowing observation of the emission from both core and core–shell NCs. A laboratory-grade fiber splitter was used to transfer emission from both optical systems to the spectrometer. The entire system was enclosed in a black box to minimize stray light pollution (see electronic supporting information, Fig. S1, ESI† for an image of the microfluidic platform).

Offline particle characterization

Toluene (300 μL) and ethanol (300 μL) were added to the crude solution followed by centrifugation to separate the synthesized NCs from the organic ligands (4500 rpm for 5 minutes). Collected NCs were redispersed in hexane, and again precipitated with ethanol for two additional washing steps and then redispersed in 300 μL of hexane. Absorption spectra and offline photoluminescence measurements for photoluminescence quantum yield estimation, were collected using Fluoromax-4 and Fluorolog iHR 320 spectrofluorimeters (Horiba, Germany). Photoluminescence quantum yields of the synthesized NCs in hexane were calculated by comparison of the integrated emission with that of a Rhodamine 6G solution in ethanol (QY = 95%, λ_{ex} = 530 nm). To avoid reabsorption of emitted light, the optical density of all samples at the excitation wavelength was kept below 0.1.

$$QY = QY_{dye} \cdot \frac{S_{QD}}{S_{dye}} \cdot \frac{Abs_{dye}}{Abs_{QD}} \cdot \frac{{n_{QD}}^2}{{n_{dye}}^2} \quad (1)$$

Here QY_{dye} is the absolute photoluminescence quantum yield for Rhodamine 6G (95% in ethanol),[55] S is the integrated area under the corrected fluorescence spectrum, Abs is the absorbance at 488 nm and n is the refractive index of toluene or ethanol. All optical measurements were performed at room temperature. X-ray diffraction measurements (XRD) (using an Oxford Excalibur Diffractometer equipped with a Sapphire CCD) were performed using MoKα radiation. XRD samples were prepared by evaporating a concentrated NC hexane suspension on a glass slide. For high-resolution transmission electron microscopy (TEM) samples were dispersed in ethanol and droplets of the suspension were deposited on a lacey carbon foil supported on a Cu grid (Okenshoji, Japan). Images of the synthesized NCs were obtained using an FEI Technai F30 microscope operated at 300 kV. An energy-dispersive X-ray spectrometer attached to this microscope (EDAX Gemini) was used to perform a qualitative elemental analysis at selected areas.

Results and discussion

Parametric screening of $CuInS_2$ nanocrystal synthesis

The integration of the droplet-based capillary reactor with in-line fluorescence detection (Fig. 1) allows the rapid screening of reaction parameters that control particle growth and the optical characteristics of the synthesized NCs. Herein we focus on the synthesis of $CuInS_2$ NCs following previously reported macroscale synthetic procedures with CuI and $In(OAc)_3$ as the metal precursors and DDT as the sulfur source and capping ligand (since it forms thiolates with various metal salts, which decompose during heating leading to the corresponding metal sulfides). Stoichiometric sulfur was additionally used to accelerate reaction kinetics by ensuring an excess of the sulfur source inside the formed droplets. In flask-based syntheses, metal precursors mixed together in an ODE solution followed by hot injection of DDT solution into the reaction mixture to form $CuInS_2$ NCs in the sub-10 nm range. However, this procedure entails the detailed investigation of compositional effects on optical properties of the particles, since metal salts are pre-mixed at defined ratios prior to injection of DDT. An important variation with respect to previously reported synthetic methods is the separation of all precursor solutions (dissolved in ODE together with OA and OLA), allowing for a precise control of precursor reactivities during the synthesis. Accordingly, parameters such as Cu/In and S/(Cu + In) molar ratios could be explored for the first time in detail.

The bandgap of $CuInS_2$ NCs is highly dependent on the Cu/In molar ratio, where "Cu-deficient" $CuInS_2$ NCs are found to have wider bandgaps. However, further investigation is required to elucidate the effects of the Cu/In ratio on physicochemical properties. Fig. 2a shows the evolution of photoluminescence emission spectra of $CuInS_2$ cores, which were prepared using Cu/In molar ratios (R_1) between 0.3 and 1.8 at 180 °C. In the current experiments, the reaction time was maintained at 15 seconds, demonstrating rapid formation of $CuInS_2$ NCs when compared to flask-based approaches (with reported reaction times between minutes and hours). Indeed, for reaction times in excess of 90 seconds we determined that reaction time is not a size-tuning parameter for the synthesis of $CuInS_2$ cores (indicating that the reaction reaches completion within a few seconds, see ESI,† Fig. S2). As observed in Fig. 2a, a systematic increase in the Cu/In molar ratio leads to a red shift in the emission spectrum from 695 to 760 nm and an associated increase in the full width at half maximum (FWHM) from 118 to 140 nm. The blue shift associated with a reduction in Cu concentration is consistent with previous reports[56,57] because of the lowering of the valence band due to the weakened repulsion between Cu d and S p orbitals in Cu-deficient nanoparticles which results in band gap widening. Monodisperse $CuInS_2$ cores, with FWHM values between 115 and 125 nm, were synthesized when the Cu/In molar ratio was varied between 0.3 and 0.4.

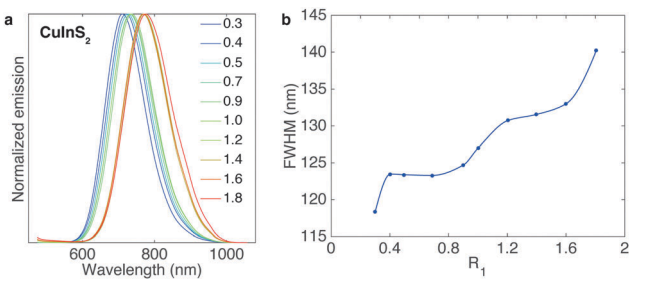

Fig. 2 Variation of (a) emission spectra and (b) FWHM of $CuInS_2$ with a systematic variation of the Cu/In (R_1) molar ratio at 180 °C. The reaction time was fixed at 14.7 s and the S/(Cu + In) (R_2) molar ratio is equal to 2.6.

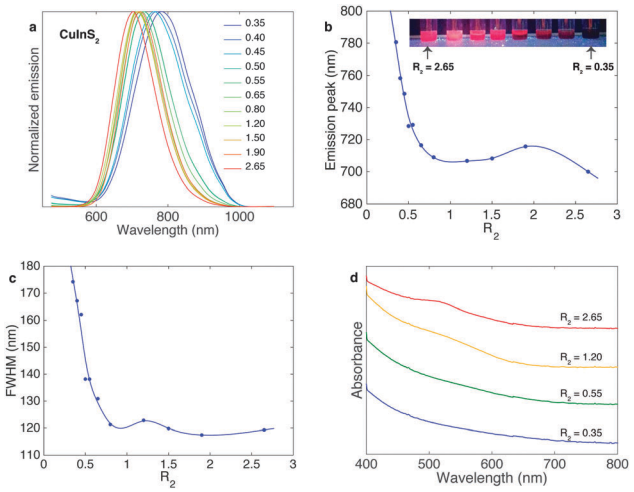

Fig. 3 Variation of (a) emission spectra, (b) emission peak wavelength and (c) FWHM of $CuInS_2$ NCs through a systematic variation of R_2 from 0.35 to 2.65. Other parameters were: R_1 = 0.4, reaction time = 14.7 s and T = 180 °C. The inset in (b) shows colloidal solutions of various $CuInS_2$ in toluene under UV lamp (λ = 365 nm) irradiation. (d) Selected absorption spectra of $CuInS_2$ NCs at various R_2 corresponding to the PL spectra.

Another critical reaction parameter affecting particle size and thus the ensuing optical properties of $CuInS_2$ cores is the molar ratio between S and (Cu + In) (R_2). For this reason, we sought to develop an improved understanding of optimum R_2 molar ratios in the synthesis of monodisperse $CuInS_2$ NCs. For all the experiments in this study, R_1 was set to 0.3, which was defined as the optimum R_1 value. Fig. 3 reports the effect of R_2 on the photoluminescence emission spectra, emission peak and FWHM and absorption characteristics. Variation of R_2 from 0.35 to 2.65 leads to a blue-shift in the band-edge emission from 780 to 700 nm (Fig. 3a and b). The inset in Fig. 3b shows emission from various $CuInS_2$ NCs formed using different R_2 molar ratios under UV illumination. Moreover, analysis of the effect of R_2 on the FWHM and absorption spectra, indicates that high values of R_2 ($\geq$1.2) lead to band edge emission of narrow linewidth (from 118 to 120 nm) and well-defined absorption peaks (see for example the absorption spectrum for an R_2 value of 2.65). Importantly, $CuInS_2$ NCs synthesized with Cu/In and S/(Cu + In) molar ratios of 0.4 and 2.65 respectively, exhibit photoluminescence quantum yields of 12.4%, which is equivalent to the highest photoluminescence quantum yields reported for flask-based syntheses over timescales of many minutes.

Parametric screening of $CuInS_2$/ZnS nanocrystal synthesis

Surface passivation of $CuInS_2$ NCs by means of epitaxial growth of a wider band-gap material (commonly ZnS) has proved to be

an efficient strategy for enhancing both stability and photoluminescence quantum yields. Although several methods have been proposed for shell addition, they have proved to be rather time-consuming and operationally complex, leading to significant batch-to-batch variabilities and offering limited possibilities for scale-up.[37,58,59] The majority of these methods are based on the dropwise addition of the shell material into a sample containing purified $CuInS_2$ cores. Alternative methods have been suggested, and involve the addition of a single source precursor that decomposes at high reaction temperatures.[60,61] Herein, we leverage a similar idea, where $Zn(OAc)_2$ thermally decomposes to ZnS. This allows for the direct injection of a Zn precursor solution ($Zn(OAc)_2$ and OLA in ODE) into droplets containing $CuInS_2$ cores, without any intermediate purification steps. In this case, Zn can be injected into the flowing droplets as a continuous laminar stream. Variation of the flow rate of the Zn precursor solution allows for the addition of user-defined concentrations of Zn, affording control over the number of ZnS monolayers introduced. Due to the large excess of the sulfur precursor during the synthesis of the $CuInS_2$ cores, no additional sulfur source was used for surface passivation. The resulting droplets were then directed into the second heating zone for further growth of the ZnS shell. Importantly, a second in-line photoluminescence detection system allowed for rapid assessment of photoluminescence variations after the formation of $CuInS_2$/ZnS NCs and thus further optimization of reaction parameters.

After identifying the optimum conditions for synthesizing high quality $CuInS_2$ cores, we then explored the amount of ZnS precursor needed to achieve monodisperse and highly luminescent $CuInS_2$/ZnS NCs, and the effect of the Zn/(Cu + In) molar ratio (R_3) on emission and absorption characteristics. Fig. 4a and b present the raw photoluminescence spectra and extracted FWHM as a function of R_3, whilst maintaining a total reaction time of 32 s. It is noticeable that overcoating with ZnS results in a dramatic increase in emission intensity when compared to the bare $CuInS_2$ cores. Moreover, an increase of the Zn/(Cu + In) molar ratio from 0.2 to 2.3 leads to the blue-shift of photoluminescence maxima from 700 (core particle emission) to 660 nm. Such a blue shift can be attributed to the combined effects of surface passivation by ZnS and shrinking of the core.[62,63] Furthermore, an increase in R_3 results in a dramatic enhancement in the emission intensity while the emission maximum remains constant. Such variations are directly accessible through integration of the in-line photoluminescence detection system and therefore allow for real-time assessment of the $CuInS_2$/ZnS NC synthesis. In addition, the FWHM of $CuInS_2$/ZnS NCs are as low as 93 nm, suggesting the formation of core–shell structures with narrower emission linewidths than those previously synthesized in batch reactors. Such narrow emission linewidths demonstrate the excellent control of reaction conditions afforded by the two-step droplet-based microfluidic platform. Although, variation of R_3 is critical in defining the emission characteristics of core–shell NCs, ZnS passivation of $CuInS_2$ has no discernable affect on absorption spectra (4*c*), thus excluding the possibility of diffusion of Zn ions into the core. Importantly, after shell growth, photoluminescence quantum yields of $CuInS_2$/ZnS NCs emitting between 635 and 690 nm exceed 40%, whereas the maximum value attained for 659 nm emitting core–shell structures was 55% (see Table 1). These results suggest that the synthesized core–shell NCs exhibit similar photoluminescence quantum yields to those synthesized in flask-based reactors. We believe that additional Zn injection steps (for the sequential growth of ZnS shells) would allow for the formation of core–shell structures with even higher stabilities and enhanced photoluminescence quantum efficiencies.

Composition and structure of the synthesized $CuInS_2$/ZnS nanocrystals

Energy dispersive spectroscopy (EDX) was used to determine the chemical composition of the synthesised NCs (see ESI,† Fig. S3)

Table 1 QY measurements of $CuInS_2$/ZnS NCs

Zn/(Cu + In)	QY (%)	Emission (nm)	FWHM (nm)
0.2	25	634	99
1.0	35	638	96
2.5	37	654	101
5.0	**55**	**659**	**93**
10.0	45	679	96

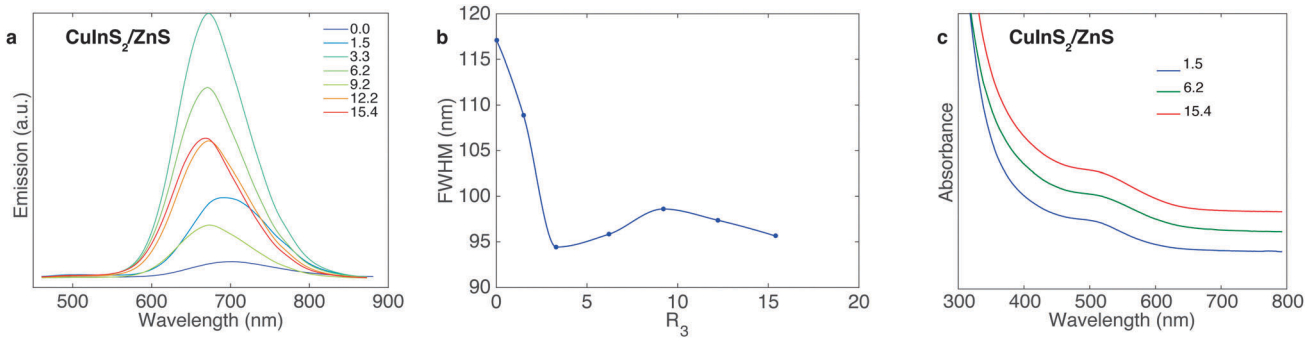

Fig. 4 The effect of Zn/(Cu + In) molar ratio (R_3) on emission and absorption characteristics of $CuInS_2$/ZnS NCs. Tuning of (a) emission spectra, (b) FWHM by a systematic variation of R_3 from 0.2 to 2.3. (c) Absorption spectra $CuInS_2$/ZnS NCs while R_3 is equal to 1, 5, and 12. Other parameters were: R_1 = 0.3, R_2 = 2.65, reaction time = 32 s, T_{core} = 180 °C and T_{shell} = 230 °C.

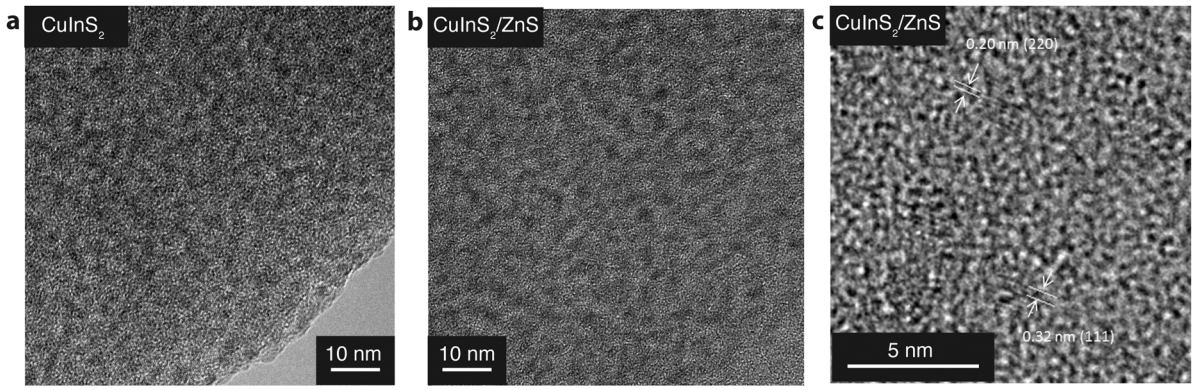

Fig. 5 TEM images of (a) $CuInS_2$ core, (b) $CuInS_2$/ZnS core/shell NCs. (c) High-resolution TEM image of $CuInS_2$/ZnS NCs showing the lattice plane spacings corresponding to the (111) and (220) planes of the cubic structure.

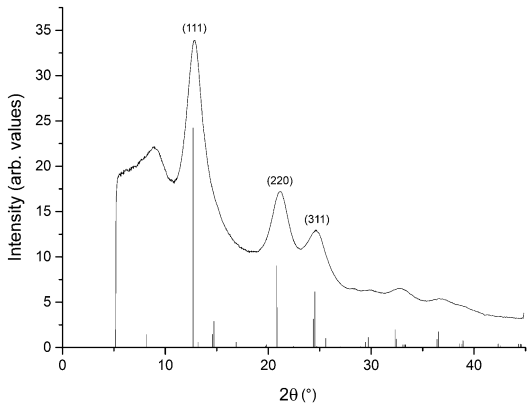

Fig. 6 XRD pattern of $CuInS_2$/ZnS core/shell NCs.

and confirmed the presence of Cu, In, S and Zn in the $CuInS_2$/ZnS core/shell NCs. TEM and powder XRD were employed to characterize the morphology and crystal structure of $CuInS_2$/ZnS. TEM images of $CuInS_2$ and $CuInS_2$/ZnS NCs are shown in Fig. 5 and indicate that they are dispersive and nearly spherical in shape (see ESI,† Fig. S4 for additional TEM images). Indeed, lattice plane spacings (Fig. 5c) of 0.32 nm and 0.2 nm correspond to the (111) and (220) planes of the cubic structure of $CuInS_2$ respectively.

The XRD pattern of the $CuInS_2$ core is relatively broad showing three distinct reflection peaks indexed to the (111), (220) and (311) planes of the cubic $CuInS_2$ structure (Fig. 6). Upon surface passivation of $CuInS_2$ cores with a ZnS shell, the pattern of the cubic lattice is maintained, and diffraction peaks become sharper and shift to marginally larger angles. These results confirm that high quality $CuInS_2$ and $CuInS_2$/ZnS NCs with a cubic structure have been synthesized successfully.

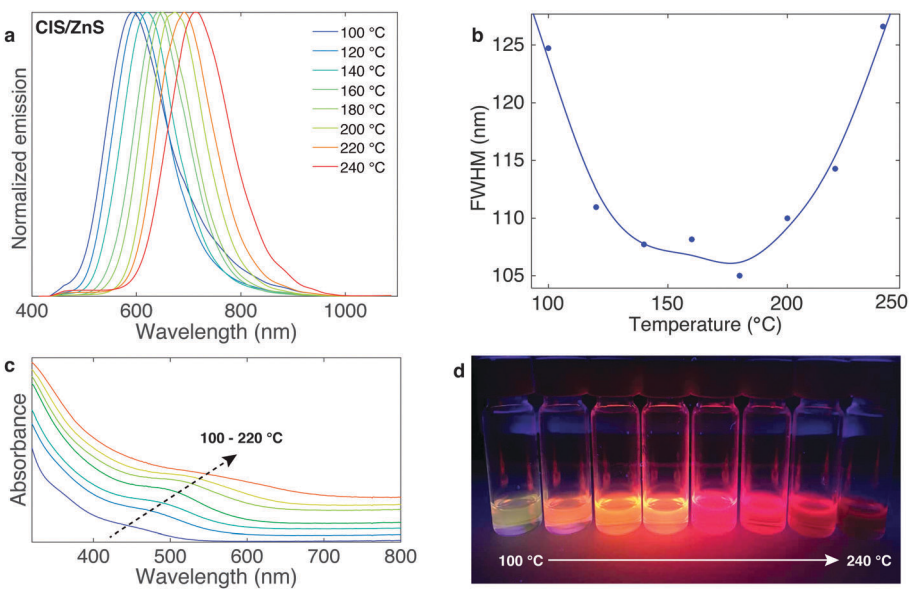

Fig. 7 The effect of the temperature of stage 1 (core NC synthesis) on (a) emission spectra, (b) FWHM and (c) absorbance spectra of $CuInS_2$/ZnS NCs. Other parameters were: R_1 = 0.4, R_2 = 2.65, R_3 = 3, reaction time = 32 s and T_{shell} = 230 °C. (d) Colloidal solutions of various $CuInS_2$/ZnS in toluene under UV lamp (λ = 365 nm).

Effect of temperature on the spectral properties

A key feature of the two-stage microfluidic platform is the ability to independently control of the temperature of the first stage (T_{core} when synthesizing the $CuInS_2$ cores) with respect to the second stage (T_{shell} when synthesizing the $CuInS_2$/ZnS core–shell NCs). This feature allows for direct tuning of emission and absorption spectra of $CuInS_2$/ZnS NCs originating from $CuInS_2$ cores with different diameters. Temperature-dependent emission and absorption spectra of the core–shell structures are shown in Fig. 7. Notably, photoluminescence emission spectra can be tuned from 580 to 760 nm by increasing T_{core} from 100 to 240 °C. Fig. 7b shows that the optimal temperature range in stage 1 that provides for a satisfactory FWHM of the band edge emission is between 140 and 200 °C. Absorbance spectra in Fig. 7c are in accordance with *in situ* photoluminescence measurements and clearly illustrate the size focusing and broadening evident in Fig. 7b.

Finally, we investigated the effect of T_{shell} on the photoluminescence properties of the core–shell structures by varying the temperature of the second stage between 150 and 230 °C. Results demonstrate minimal emission tuning *via* a variation in T_{shell}, suggesting complete shell growth even at temperatures below 200 °C. Emission intensities were higher for NCs synthesized at a T_{shell} of 230 °C (Fig. S5, ESI†), however reactions at temperatures higher than 230 °C led to the formation of large aggregates.

Conclusions

We have designed a two-stage droplet-based microfluidic platform with integrated photoluminescence detection for the synthesis of $CuInS_2$/ZnS NCs, that allows for the rapid screening of reaction parameters controlling core and shell synthesis. The two stage microfluidic platform allows for ZnS passivation of the $CuInS_2$ cores without the need for any intermediate purification steps and affords the rapid production of high-quality $CuInS_2$ and $CuInS_2$/ZnS NCs with photoluminescence quantum yields reaching 12 and 55% respectively. Moreover, we have shown for the first time that compositional screening of the core and core–shell structures enables the facile identification of optimum reaction conditions for the synthesis of "monodisperse" $CuInS_2$/ZnS NCs with FWHMs between 90 and 95 nm. Stable core–shell structures emitting between 580 and 760 nm were synthesized by individual assessment of reaction temperatures at the two positions. Adoption of the proposed methodology could further improve the photoluminescence quantum efficiency of similarly synthesized NCs through multi-step addition of the Zn precursor during the second heating stage. This would allow for sequential growth of the shell material leading to core–shell structures containing a defined number of monolayers. Finally but significantly, high-throughput production of high-quality ternary and core–shell ternary-binary NCs possessing narrow size distributions can be produced using a scaled out version of the proposed two-stage platform. This would eventually boost the production of efficient non-heavy metal QDs in large volumes, which is expected to advance the adoption of semiconductor nanocrystals in lighting and display applications.

Acknowledgements

We would like to thank Dr Frank Krumeich for performing the HRTEM analysis as well as the elemental analysis of single particles and Dr Michael Worle for XRD measurements. This work was partially supported by a National Research Foundation (NRF) grant funded by the Ministry of Science, ICT and Future Planning (MSIP) of Korea through Global Research Laboratory (GRL) Program (Grant number 2009-00426).

References

1 M. V. Kovalenko, L. Manna, A. Cabot, Z. Hens, D. V. Talapin, C. R. Kagan, V. I. Klimov, A. L. Rogach, P. Reiss, D. J. Milliron, P. Guyot-Sionnnest, G. Konstantatos, W. J. Parak, T. Hyeon, B. A. Korgel, C. B. Murray and W. Heiss, *ACS Nano*, 2015, **9**, 1012–1057.
2 J. Q. Grim, L. Manna and I. Moreels, *Chem. Soc. Rev.*, 2015, **44**, 5897–5914.
3 D. Aldakov, A. Lefrancois and P. Reiss, *J. Mater. Chem. C*, 2013, **1**, 3756–3776.
4 T. Kino, T. Kuzuya, K. Itoh, K. Sumiyama, T. Wakamatsu and M. Ichidate, *Mater. Trans.*, 2008, **49**, 435–438.
5 K. Nose, Y. Soma, T. Omata and S. Otsuka-Yao-Matsuo, *Chem. Mater.*, 2009, **21**, 2607–2613.
6 R. Xie, M. Rutherford and X. Peng, *J. Am. Chem. Soc.*, 2009, **131**, 5691–5697.
7 M. Kruszynska, H. Borchert, J. Parisi and J. Kolny-Olesiak, *J. Am. Chem. Soc.*, 2010, **132**, 15976–15986.
8 T. Pons, E. Pic, N. Lequeux, E. Cassette, L. Bezdetnaya, F. Guillemin, F. Marchal and B. Dubertret, *ACS Nano*, 2010, **4**, 2531–2538.
9 J. S. Niezgoda, M. A. Harrison, J. R. McBride and S. J. Rosenthal, *Chem. Mater.*, 2012, **24**, 3294–3298.
10 W.-S. Song and H. Yang, *Chem. Mater.*, 2012, **24**, 1961–1967.
11 S. D. Perera, H. Zhang, X. Ding, A. Nelson and R. D. Robinson, *J. Mater. Chem. C*, 2015, **3**, 1044–1055.
12 A. Tang, Z. Hu, Z. Yin, H. Ye, C. Yang and F. Teng, *Dalton Trans.*, 2015, **44**, 9251–9259.
13 B. Chen, S. Chang, D. Li, L. Chen, Y. Wang, T. Chen, B. Zou, H. Zhong and A. L. Rogach, *Chem. Mater.*, 2015, **27**, 5949–5956.
14 K. Nose, T. Omata and S. Otsuka-Yao-Matsuo, *J. Phys. Chem. C*, 2009, **113**, 3455–3460.
15 H. Zhong, Z. Wang, E. Bovero, Z. Lu, F. C. J. M. van Veggel and G. D. Scholes, *J. Phys. Chem. C*, 2011, **115**, 12396–12402.
16 H. Zhong, Y. Li, M. Ye, Z. Zhu, Y. Zhou, C. Yang and Y. Li, *Nanotechnology*, 2007, **18**, 025602.
17 E. Cassette, T. Pons, C. Bouet, M. Helle, L. Bezdetnaya, F. Marchal and B. Dubertret, *Chem. Mater.*, 2010, **22**, 6117–6124.

18 X. Kang, Y. Yang, L. Huang, Y. Tao, L. Wang and D. Pan, *Green Chem.*, 2015, **17**, 4482–4488.
19 X. Tang, K. Yu, Q. Xu, E. S. G. Choo, G. K. L. Goh and J. Xue, *J. Mater. Chem.*, 2011, **21**, 11239–11243.
20 W.-W. Xiong, G.-H. Yang, X.-C. Wu and J.-J. Zhu, *J. Mater. Chem. B*, 2013, **1**, 4160–4165.
21 M. Deng, S. Shen, X. Wang, Y. Zhang, H. Xu, T. Zhang and Q. Wang, *CrystEngComm*, 2013, **15**, 6443–6447.
22 X. Kang, L. Huang, Y. Yang and D. Pan, *J. Phys. Chem. C*, 2015, **119**, 7933–7940.
23 C. Coughlan and K. M. Ryan, *CrystEngComm*, 2015, **17**, 6914–6922.
24 R. Ahmad, M. Brandl, M. Distaso, P. Herre, E. Spiecker, R. Hock and W. Peukert, *CrystEngComm*, 2015, **17**, 6972–6984.
25 B. D. Chernomordik, A. E. Beland, N. D. Trejo, A. A. Gunawan, D. D. Deng, K. A. Mkhoyan and E. S. Aydil, *J. Mater. Chem. A*, 2014, **2**, 10389–10395.
26 A. Shavel, D. Cadavid, M. IbÃČÂąÃČÂśez, A. Carrete and A. Cabot, *J. Am. Chem. Soc.*, 2012, **134**, 1438–1441.
27 J. Kolny-Olesiak and H. Weller, *ACS Appl. Mater. Interfaces*, 2013, **5**, 12221–12237.
28 D. Deng, Y. Chen, J. Cao, J. Tian, Z. Qian, S. Achilefu and Y. Gu, *Chem. Mater.*, 2012, **24**, 3029–3037.
29 B. Chen, H. Zhong, W. Zhang, Z. Tan, Y. Li, C. Yu, T. Zhai, Y. Bando, S. Yang and B. Zou, *Adv. Funct. Mater.*, 2012, **22**, 2081–2088.
30 W.-S. Song and H. Yang, *Chem. Mater.*, 2012, **24**, 1961–1967.
31 S. H. Park, A. Hong, J.-H. Kim, H. Yang, K. Lee and H. S. Jang, *ACS Appl. Mater. Interfaces*, 2015, **7**, 6764–6771.
32 G. Niu, A. Ruditskiy, M. Vara and Y. Xia, *Chem. Soc. Rev.*, 2015, **44**, 5806–5820.
33 T. W. Phillips, I. G. Lignos, R. M. Maceiczyk, A. J. deMello and J. C. deMello, *Lab Chip*, 2014, **14**, 3172–3180.
34 R. Xie, U. Kolb, J. Li, T. Basch and A. Mews, *J. Am. Chem. Soc.*, 2005, **127**, 7480–7488.
35 K. F. Jensen, B. J. Reizman and S. G. Newman, *Lab Chip*, 2014, **14**, 3206–3212.
36 K. S. Elvira, X. C. i Solvas, R. C. R. Wootton and A. J. deMello, *Nat. Chem.*, 2013, **5**, 905–915.
37 M. S. Naughton, V. Kumar, Y. Bonita, K. Deshpande and P. J. A. Kenis, *Nanoscale*, 2015, **7**, 15895–15903.
38 S. G.-d. Pedro, M. Puyol, D. Izquierdo, I. Salinas, J. M. de la Fuente and J. Alonso-Chamarro, *Nanoscale*, 2012, **4**, 1328–1335.
39 H. Yang, W. Luan, Z. Wan, S. tung Tu, W.-K. Yuan and Z. M. Wang, *Cryst. Growth Des.*, 2009, **9**, 4807–4813.
40 P. Laurino, R. Kikkeri and P. H. Seeberger, *Nat. Protoc.*, 2011, **6**, 1209–1220.
41 B.-H. Kwon, K. G. Lee, T. J. Park, H. Kim, T. J. Lee, S. J. Lee and D. Y. Jeon, *Small*, 2012, **8**, 3257–3262.
42 K. Kim, S. Jeong, J. Y. Woo and C.-S. Han, *Nanotechnology*, 2012, **23**, 065602.
43 J. Lee and C.-S. Han, *Nanoscale Res. Lett.*, 2014, **9**, 78.
44 S. Li, Y. Chen, L. Huang and D. Pan, *Nanotechnology*, 2013, **24**, 395705.
45 R. M. Maceiczyk and A. J. deMello, *J. Phys. Chem. C*, 2014, **118**, 20026–20033.
46 M. Abolhasani, C. W. Coley, L. Xie, O. Chen, M. G. Bawendi and K. F. Jensen, *Chem. Mater.*, 2015, **27**, 6131–6138.
47 I. Lignos, L. Protesescu, S. Stavrakis, L. Piveteau, M. J. Speirs, M. A. Loi, M. V. Kovalenko and A. J. deMello, *Chem. Mater.*, 2014, **26**, 2975–2982.
48 I. Lignos, S. Stavrakis, A. Kilaj and A. J. deMello, *Small*, 2015, **11**, 4009–4017.
49 I. Lignos, S. Stavrakis, G. Nedelcu, L. Protesescu, A. J. deMello and M. V. Kovalenko, *Nano Lett.*, 2016, **16**, 1869–1877.
50 X. Niu, S. Gulati, J. B. Edel and A. J. deMello, *Lab Chip*, 2008, **8**, 1837–1841.
51 A. R. Abate, T. Hung, P. Mary, J. J. Agresti and D. A. Weitz, *Proc. Natl. Acad. Sci. U. S. A.*, 2010, **107**, 19163–19166.
52 A. M. Nightingale, T. W. Phillips, J. H. Bannock and J. C. de Mello, *Nat. Commun.*, 2014, **5**, 3777.
53 J. M. Koehler, S. Li and A. Knauer, *Chem. Eng. Technol.*, 2013, **36**, 887–899.
54 I. Shestopalov, J. D. Tice and R. F. Ismagilov, *Lab Chip*, 2004, **4**, 316–321.
55 L. Qu and X. Peng, *J. Am. Chem. Soc.*, 2002, **124**, 2049–2055.
56 M. Uehara, K. Watanabe, Y. Tajiri, H. Nakamura and H. Maeda, *J. Chem. Phys.*, 2008, **129**, 134709.
57 D.-E. Nam, W.-S. Song and H. Yang, *J. Colloid Interface Sci.*, 2011, **361**, 491–496.
58 J. J. Li, Y. A. Wang, W. Guo, J. C. Keay, T. D. Mishima, M. B. Johnson and X. Peng, *J. Am. Chem. Soc.*, 2003, **125**, 12567–12575.
59 W. K. Bae, M. K. Nam, K. Char and S. Lee, *Chem. Mater.*, 2008, **20**, 5307–5313.
60 T. Trindade, P. O'Brien and X.-m. Zhang, *Chem. Mater.*, 1997, **9**, 523–530.
61 H. Wang, H. Nakamura, M. Uehara, Y. Yamaguchi, M. Miyazaki and H. Maeda, *Adv. Funct. Mater.*, 2005, **15**, 603–608.
62 L. Li, A. Pandey, D. J. Werder, B. P. Khanal, J. M. Pietryga and V. I. Klimov, *J. Am. Chem. Soc.*, 2011, **133**, 1176–1179.
63 Y.-K. Kim, S.-H. Ahn, K. Chung, Y.-S. Cho and C.-J. Choi, *J. Mater. Chem.*, 2012, **22**, 1516–1520.

